




Self-doping behavior and cation disorder in MgSnN_2

Dan Han ^{*}, Stefan S. Rudel , Wolfgang Schnick , and Hubert Ebert

Department of Chemistry, University of Munich, Butenandtstrasse 5-13, D-81377 Munich, Germany



(Received 14 October 2021; revised 11 March 2022; accepted 11 March 2022; published 28 March 2022)

Investigations on II-Sn-N₂ (II = Mg, Ca) have been started very recently compared to the intense research of Zn-IV-N₂ (IV = Si, Ge, Sn). In this work, we study the phase stability of MgSnN_2 and ZnSnN_2 in wurtzite and rocksalt phases by first principles calculations. The calculated phase diagram agrees with the experimental observation; i.e., MgSnN_2 can form in the wurtzite and rocksalt phases while ZnSnN_2 only crystallizes in the wurtzite phase. Due to the higher ionicity of Mg-N bonds compared to Sn-N bonds and Zn-N bonds, wurtzite-type MgSnN_2 appears under Mg-rich conditions. The defect properties and doping behavior of MgSnN_2 in the wurtzite phase are further investigated. We find that MgSnN_2 exhibits self-doped *n*-type conductivity, and donor-type antisite defect Sn_{Mg} is the primary source of free electrons. The high possibility of forming the stoichiometry-preserving $\text{Mg}_{\text{Sn}} + \text{Sn}_{\text{Mg}}$ defect complex leads to our study of cation disorder in MgSnN_2 by using the cluster expansion method with first principles calculations. It is found that cation disorder in MgSnN_2 induces a band-gap reduction because of a violation of the octet rule. The local disorder, namely, forming (4,0) or (0,4) tetrahedra, leads to an appreciable band-gap reduction and hinders the enhancement of the optical absorption.

DOI: [10.1103/PhysRevB.105.125202](https://doi.org/10.1103/PhysRevB.105.125202)

I. INTRODUCTION

Binary nitride semiconductors and related alloys have wide applications, such as high-power and light emitting devices [1–5]. As analogs to binary nitride semiconductors, ternary nitride semiconductors have recently drawn immense attention because of their richer composition space and potentially wider applications [6–10]. Among them, the Zn-IV-N₂ (IV = Si, Ge, Sn) series and their alloys have been under intense exploration [11–15]. Due to the beneficial characteristics, viz., earth abundant composition, suitable band gap, and benign defect properties [6,9,11], ZnSnN_2 has gained special interest, which has been proposed as a potential photovoltaic absorber [9]. However, it was lately identified that ZnSnN_2 suffers from a degenerate electron concentration (10^{18} – 10^{21} cm^{−3}) no matter whether synthesized as bulk by a high-pressure metathesis reaction or as thin films grown by molecular beam epitaxy (MBE) or sputtering [8,9,16–18]. Such high concentration of electron carriers can change the onset of the light absorption spectrum due to the Burstein-Moss effect [8,9] and exceed the optimal range of carrier concentration for photovoltaic application (10^{16} – 10^{18} cm^{−3}) [19,20], which indicates that ZnSnN_2 may be unsuitable for photovoltaic application. Nevertheless, ZnSnN_2 based photovoltaic devices have been fabricated, but they show low power conversion efficiency of 1.54% [21,22]. However, solutions to reduce the carrier density in ZnSnN_2 are still under investigation because of its aforementioned natural advantages [23–25]. It is experimentally demonstrated that both the Zn-rich condition and low-temperature growth are beneficial for suppressing the carrier concentration [23]. A degenerate electron behavior is also found in ZnGeN_2 [26,27] but a corresponding finding has not been reported yet for ZnSiN_2 .

In contrast to the intense research on Zn-IV-N₂ (IV = Si, Ge, Sn), studies on II-Sn-N₂ (II = Mg, Ca) have been started only recently [28–34]. The electronic properties of MgSnN_2 were studied first by Jaroenjittichai and Lambrecht [28], with a band gap predicted close to 3.4 eV while their recent work revised the band gap of MgSnN_2 to be 2.3 eV after including Sn-4*d* semicore states [29]. Nonetheless, the cation disorder of MgSnN_2 remains insufficiently explored, which is expected to have an important effect on the band gaps according to preceding studies of Zn-IV-N₂ (IV = Si, Ge, Sn); i.e., cation disorder strongly influences their electronic structure [13,35]. Experimentally, Greenaway *et al.* prepared MgSnN_2 thin films with a broad range of cation compositions and gave a phase map of samples under different Mg/Sn ratios and temperatures [31]. Apart from the wurtzite-type phase, this map shows in particular that a rocksalt-type phase appears under Mg-rich conditions, which has not been observed in ZnSnN_2 and ZnGeN_2 under Zn-rich conditions [24,36]. Additionally, MgSnN_2 crystallizes in the rocksalt-type structure by using a metathesis reaction under high pressure whereas ZnSnN_2 crystallizes in the wurtzite-type structure when using the same preparation method [32,33]. This leads to the question of why MgSnN_2 can appear in the rocksalt-type phase while ZnSnN_2 and ZnGeN_2 appear only in the wurtzite-type phase. It is still an open question to date, which will be addressed in this study. In addition, high electron densities in Sn-rich MgSnN_2 ($\sim 10^{20}$ cm^{−3}) and in Mg-rich samples ($\sim 10^{18}$ cm^{−3}) have been reported recently, which shows a similar degenerate behavior to ZnSnN_2 . However, the origin of high electron density is not clear.

In this work, we study the phase stability of MgSnN_2 and ZnSnN_2 in the wurtzite and rocksalt phases, and investigate defect properties of MgSnN_2 in the wurtzite phase via first principles calculations. Donor-type antisite defect Sn_{Mg} is identified as the primary source of high electron carriers, which leads to self-doped *n*-type conductivity of MgSnN_2

^{*}Dan.Han@cup.uni-muenchen.de

under Mg-poor/Sn-rich and Mg-rich/Sn-poor condition. By changing the chemical potential of the growth environment from Mg-poor/Sn-rich to Mg-rich/Sn-poor, the calculated density of electrons is reduced by an order of magnitude of 3. Moreover, we perform a comprehensive investigation of cation disorder in MgSnN_2 by using the cluster expansion method with first principles calculations. It is found that cation disorder in MgSnN_2 induces a band-gap reduction because of the formation of motifs violating the octet rule, which is similar to the cases of ZnSnN_2 and ZnGeN_2 .

II. CALCULATION METHODOLOGY

The MgSnN_2 in the $\beta\text{-NaFeO}_2$ structure type with the space group $Pna2_1$ (no. 33) is more stable than that wurtzite-type phase with space group $P2/c$ (no. 13), as suggested by Ref. [31]. Both crystal structures obey the local octet rule. The geometry optimization, calculations of total energy, and electronic structure were performed within the framework of density functional theory via the Vienna *ab initio* simulation package (VASP) [37–39]. The projected augmented wave pseudopotential was utilized to describe the ion-electron interaction [40,41]. The following electron configurations were treated as valence electrons: Mg ($2p^63s^2$), Sn ($4d^{10}5s^25p^2$), N ($2s^22p^3$), and Zn ($3d^{10}4s^2$). A 520 eV energy cutoff of a plane-wave basis was used for all calculations. The convergence criterion for the energy and the force were set at 10^{-5} eV and 0.01 eV/Å, respectively. The Perdew-Burke-Ernzerhof exchange-correlation functional revised for solids (PBEsol) within the generalized gradient approximation (GGA) was employed [42]. PBEsol can describe the lattice parameters well; i.e., in most cases, the lattice parameters relaxed by PBEsol are close to the experimental values [43–45].

Formation energies and transition levels of defects are cell-size and k -sample dependent. It has been revealed that a 128-atom supercell based on the $\beta\text{-NaFeO}_2$ structure type with a $2 \times 2 \times 2$ Monkhorst-Pack k point for calculating the defect properties of ZnSnN_2 gives reasonable results [19,46]. The same setting is adopted for defect properties calculation of MgSnN_2 herein. Formation energies and transition levels are calculated by using the formula given in Refs. [47–49]. To correct the band gap from GGA, the hybrid function is one of the best choices [50], which combines good accuracy with a feasible numerical cost. Thus, we employed HSE06 with standard 25% exact Fock exchange for the total energy calculations for intrinsic point defects and defect complexes of which the structures are optimized by PBEsol (named the PBEsol-HSE procedure). The geometry optimization is recommended to be carried out by HSE06 for higher accuracy [51]. However, the evaluation of formation energies of all defects in MgSnN_2 by hybrid functional throughout (called the HSE-HSE procedure) is currently out of our computational capacity. For a benchmark, we only employed the HSE-HSE procedure to calculate the formation energies of the dominant donor defect Sn_{Mg} . Corresponding discussion is given in Sec. III C. The potential alignment and image charge corrections are applied to defect formation energies by using the method described in Ref. [52]. Fermi level, defect, and carrier densities are calculated by self-consistently solving the charge neutrality conditions [53], of which 773 and 300 K are were

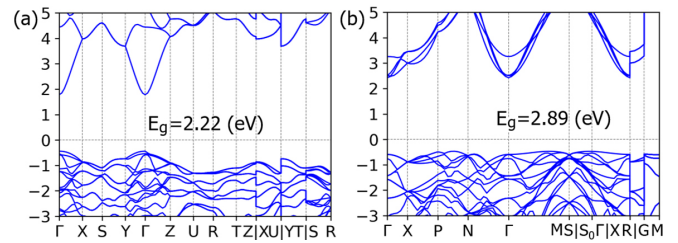


FIG. 1. Band structures of MgSnN_2 in the (a) wurtzite phase [space group (SG) $Pna2_1$] and rocksalt phase [space group (SG) $P2/c$], respectively.

considered as growth temperature and measuring temperature [31,33,34]. The binding energy (E_b) of a defect complex is calculated by

$$E_b = E_{AB} + E_P - E_A - E_B, \quad (1)$$

where E_{AB} , E_P , E_A , and E_B are the total energies of the defect complex $A + B$, host supercell without any defect, supercell with isolated defect A and supercell with isolated defect B , respectively [54]. The calculated negative (positive) binding energy represents for attraction (repulsion) for defect complex. E_b represents the binding energy of one point defect attached to a defect pair for defect triplets.

Different levels of cation disorder for MgSnN_2 were considered (see Sec. III D), which starts from the $\beta\text{-NaFeO}_2$ structure type with the space group $Pna2_1$. Accordingly, 128-atom supercells with different levels of cation disorder were generated by the cluster expansion method [55,56] by using the MCSQS code implemented in the Alloy Theoretic Automated Toolkit (ATAT) [57]. Two shells for pairs and triplets were considered. HSE06 was employed for the electronic structure of an ordered compound and disordered compounds as well. The absorption coefficient spectra of fully ordered and three partially disordered stoichiometric MgSnN_2 samples were calculated using a denser k -point mesh (less than $2\pi \times 0.01 \text{ \AA}^{-1}$).

III. RESULTS AND DISCUSSION

A. Electronic structure of MgSnN_2

It was reported that MgSnN_2 crystallizes in the wurtzite phase when grown by the sputtering method [31,34]. Besides the wurtzite-type crystal structure, MgSnN_2 can crystallize in the rocksalt-type phase by a metathesis reaction under high pressure [32,33] even though the rocksalt-type phase is energetically much less favorable than the wurtzite-type phase [31]. Therefore, we calculated the band structures for both phases, namely, $Pna2_1$ (no. 33) for the wurtzite and $P2/c$ (no. 13) for the rocksalt-type phase. As shown in Fig. 1, MgSnN_2 in the $Pna2_1$ phase exhibits a direct band gap (2.22 eV) at the Γ point while MgSnN_2 in the $P2/c$ phase shows an indirect band gap (2.89 eV) with valence band maximum (VBM) at a point along the P - N path and conduction band minimum (CBM) at the Γ point. Both phases show a common characteristic; i.e., the dispersion of the conduction band (CB) is large whereas the dispersion of the valence band (VB) is relatively small, suggesting potentially better electron transport than hole transport. Our calculated results for the band

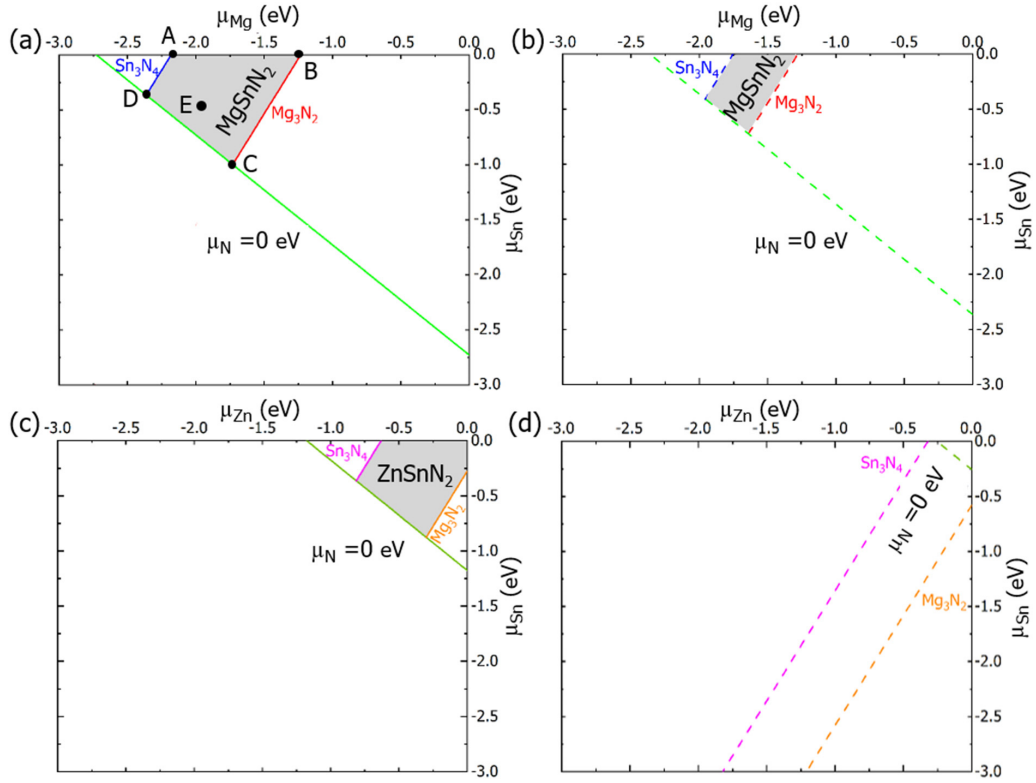


FIG. 2. Phase diagram displaying the chemical potential regions of MgSnN_2 in the (a) wurtzite and (b) rocksalt phase, respectively, and ZnSnN_2 in the (c) wurtzite and (d) rocksalt phase, respectively. The existence of the gray polygon region represents the stability of the compound. Points A–E in (a) correspond to Mg-poor/Sn-rich/N-moderate ($\mu_{\text{Mg}} = -2.18$ eV; $\mu_{\text{Sn}} = 0$ eV; $\mu_{\text{N}} = -0.27$ eV), Mg-rich/Sn-rich/N-poor ($\mu_{\text{Mg}} = -1.23$ eV; $\mu_{\text{Sn}} = 0$ eV; $\mu_{\text{N}} = -0.75$ eV), Mg-rich/Sn-poor/N-rich ($\mu_{\text{Mg}} = -1.73$ eV; $\mu_{\text{Sn}} = -1.00$ eV; $\mu_{\text{N}} = 0$ eV), Mg-poor/Sn-rich/N-rich ($\mu_{\text{Mg}} = -2.36$ eV; $\mu_{\text{Sn}} = -0.37$ eV; $\mu_{\text{N}} = 0$ eV), and Mg-moderate/Sn-moderate/N-moderate ($\mu_{\text{Mg}} = -1.96$ eV; $\mu_{\text{Sn}} = -0.50$ eV; $\mu_{\text{N}} = -0.14$ eV) conditions.

gap (HSE06) agree with previous *GW* calculations [29,31] but they are both larger than the corresponding experimental values (~ 2.0 eV for the wurtzite and 2.3 eV for the rocksalt-type phase) [31,33]. One possible reason for this disparity can be the band-gap reduction induced by the cation disorder in the synthesized samples.

B. Phase stability of MgSnN_2 and ZnSnN_2

Figure 2 displays the calculated phase diagram of MgSnN_2 (wurtzite and rocksalt phases) and ZnSnN_2 (wurtzite and rocksalt phases) as a function of the elemental chemical potentials. Under equilibrium conditions, MgSnN_2 and ZnSnN_2 in ground-state structure, i.e., the wurtzite phase (SG *Pna2*₁), are thermodynamically stable as revealed by the gray shading in Figs. 2(a) and 2(c). MgSnN_2 in the rocksalt phase (SG *P2*/*c*) is also stable but has a narrower stable region than MgSnN_2 in the wurtzite phase, as shown in Figs. 2(a) and 2(b). In contrast, there is no chemical potential region that can stabilize ZnSnN_2 in the rocksalt phase [see Fig. 2(d)] because of its largely increased formation enthalpy (ΔH_f) (-0.26 eV/f.u.) compared to that of ZnSnN_2 in the wurtzite phase (-1.18 eV/f.u.). Our calculated formation enthalpy of ZnSnN_2 in the wurtzite phase is smaller than the value (-2.32 eV/f.u.) calculated by Punya *et al.* [58] but larger than that (-0.20 eV/f.u.) reported by Pan *et al.* [46]. We employed a density functional theory (DFT) energy correction scheme for anions since

electron self-interaction in compounds with localized electronic states results in systematic errors in the DFT description of certain anions [59,60]. For the reliability of this correction scheme, comparisons between experimental and calculated formation enthalpies for other compounds are made, that is, $\Delta H_f(\text{GaN}) = -1.32$ eV/f.u. (experiment: -1.14 eV/f.u.) and $\Delta H_f(\text{Li}_3\text{N}) = -1.84$ eV/f.u. (experiment: -1.72 eV/f.u.) [60].

As mentioned above, MgSnN_2 can crystallize in the rocksalt-type structure by using a metathesis reaction under high pressure while ZnSnN_2 does not crystallize in the rocksalt-type structure no matter under which kind of synthesis conditions are present [32]. Our calculated phase diagram agrees with these experimental observations. Moreover, MgSnN_2 in the rocksalt-type phase only appears in the Mg-rich region while no ZnSnN_2 in the rocksalt-type phase exists in the Zn-rich region [24]. These behaviors can be ascribed to the ionicity of the bond; i.e., the stronger the ionic bond is, the more likely it is for a compound to form a structure with a high degree of coordination [32]. Here, the electron localization function (ELF) is employed to describe the bonding characteristic. As shown in Figs. 3(a) and 3(b), electrons are more delocalized around the Mg atom than the Sn (Zn) atom. The one-dimensional (1D) profile along the Mg–N bond [Fig. 3(c)] shows the characteristic of mixed ionic-covalent bonding [51,52]; i.e., the ELF minimum is above zero in the non-nuclear region (> 0.05). The 1D profiles

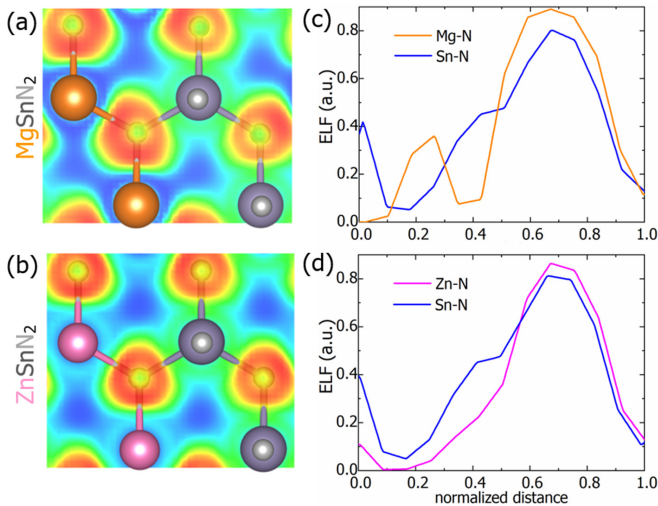


FIG. 3. Two-dimensional electron localization function (ELF) contours of (a) MgSnN_2 and (b) ZnSnN_2 and 1D profile of ELF along the (c) Mg-N and Sn-N bond and (d) Zn-N and Sn-N bond, respectively. Corresponding color code for constituents are shown on the left of (a), (b).

along the Sn-N bond [Figs. 3(c) and 3(d)] and the Zn-N bond [Fig. 3(d)] show one basin between the core of Sn (Zn) and the core of N, and the ELF maximum has moved to the position of the N atom because of the larger electronegativity of N, which shows the characteristic of covalent bonding. Thus, MgSnN_2 is able to form highly coordinated structures such as the rocksalt phase under Mg-rich condition and a tetracoordinated structure like the wurtzite phase under Sn-rich conditions. On the contrary, ZnSnN_2 tends to form a tetracoordinated structure like the wurtzite phase under both Zn-rich and Sn-rich conditions.

C. Defect physics of MgSnN_2

Studying defect properties of semiconductors is crucial for figuring out their doping behavior [27,61–65]. In this section, we focus on the intrinsic point defects and defect complexes of MgSnN_2 in the wurtzite phase. Since oxygen containment is ubiquitous in nitrides [31,66], antisite O_N and interstitial O_i are considered as well. Chemical potential points A and C in Fig. 2(a) are chosen for calculating formation energies as chemical potentials at these two points exhibit the largest disparity between the Mg and Sn chemical potentials and an acceptable small difference for the N chemical potential; these represent the Mg-poor/Sn-rich and Mg-rich/Sn-poor conditions, respectively. Under both chemical potential conditions, there are eleven donors, viz., V_N , Mg_N , Sn_Mg , Sn_N , N_Mg , N_Sn , Mg_i , Sn_i , N_i , O_N , and O_i , while there are only three acceptors, namely, V_Mg , V_Sn , and Mg_Sn in MgSnN_2 .

Under Mg-poor/Sn-rich conditions [corresponding to point A in Fig. 2(a)], cation-cation antisite Sn_Mg has the lowest formation energy within the entire Fermi level range. Sn_Mg is resonant with the CB, without transition levels (0/+ and (0/2+)) in the band gap, denoting that Sn_Mg will be ionized and generate free electron carriers once it forms. O_N and V_N are resonant in the conduction as well while they have higher

formation energies than Sn_Mg in the whole Fermi level range. Mg_Sn is the sole acceptor with formation energy lower than 3 eV when the Fermi level is close to the CB. In contrast to donor-type defects Sn_Mg , O_N , and V_N with shallow transition levels, acceptor-type defect Mg_Sn shows two deep transition levels (2 – /–) and (–/0) within the band gap. These localized transition levels can be figured out by analyzing the component of the electronic structure. As revealed by previous studies [28,67], the VB of MgSnN_2 is mainly contributed by N 2p and Sn 5d bonding states, and its CB is composed of N 2s, N 2p, and Sn 5s antibonding states. When Sn is replaced by Mg, the Sn-N bonds are broken and N 2p and Sn 5d hybridized bonding states in the VB are pushed up into the band gap, forming the deep transition levels in the band gap. For other defects, i.e., cation-anion antisite (Mg_N , Sn_N), anion-cation antisite (N_Sn , N_Mg), cation vacancy (V_Mg , V_Sn), and cation interstitial defect (Sn_i), their neutral states have rather high formation energies (above 5 eV), corresponding to an extremely low population of defects (at the order of 10^{-11} cm^{-3} estimated by the formula of equilibrium concentration given in Refs. [61,62]). Indeed, as shown in the top panel of Fig. 4(c), only Sn_Mg^{2+} , Sn_Mg^+ , O_N^+ , V_N^+ , and Mg_Sn^{2-} show appreciable densities under Mg-poor/Sn-rich condition, viz., at the order of 10^{17} cm^{-3} , 10^{18} cm^{-3} , 10^{14} cm^{-3} , 10^{10} cm^{-3} , and 10^8 cm^{-3} , respectively. Under the same condition, the calculated density of electrons reaches $4.8 \times 10^{18} \text{ cm}^{-3}$ while the calculated density of holes is rather low ($\ll 1 \text{ cm}^{-3}$). The calculated Fermi level enters into the CB with 0.05 eV above the CBM, which suggests that MgSnN_2 is a degenerate semiconductor under the Mg-rich/Sn-poor condition. Taken together, shallow donor-type defect Sn_Mg is the predominant defect, of which charged states contribute to the n-type conductivity under Mg-poor/Sn-rich condition.

Via changing the chemical potential of the elements (from the Mg-poor/Sn-rich condition to the Mg-rich/Sn-poor condition), the formation energy of shallow dominant donor-type defect Sn_Mg increases but that of acceptor-type Mg_Sn decreases. The densities of Sn_Mg^{2+} and Sn_Mg^+ reduce to $2.1 \times 10^{15} \text{ cm}^{-3}$ and $3.6 \times 10^{12} \text{ cm}^{-3}$, respectively, and that of Mg_Sn^{2-} increases by $1.2 \times 10^{11} \text{ cm}^{-3}$. Mg_Sn acceptor compensates Sn_Mg donor, which leads to the Fermi level pinning close to the CB. Indeed, the Fermi level calculated by self-consistently solving the charge neutrality conditions is only 0.16 eV below the CBM, which shows the intrinsic n-type conductivity of MgSnN_2 under Mg-rich/Sn-poor condition as well. Owing to this compensation, the density of electron carriers reduces to $4.2 \times 10^{15} \text{ cm}^{-3}$.

It was reported that Sn-rich MgSnN_2 samples had electron densities on the order of 10^{20} cm^{-3} and the electron density value of Mg-rich samples reached $7 \times 10^{18} \text{ cm}^{-3}$. Our calculated electron densities are two and three orders of magnitude lower than the experimentally measured values under Mg-poor/Sn-rich and Mg-rich/Sn-poor conditions, respectively. Notably, the measured samples were grown with nonequilibrium deposition techniques involving activated nitrogen, whereas our calculated values are under thermodynamic equilibrium conditions, which may lead to the disparity of the electron densities. The defect properties are closely related to the exchange-correlation functional because of the commonly underestimated DFT band gap. Besides the PBEsol-HSE

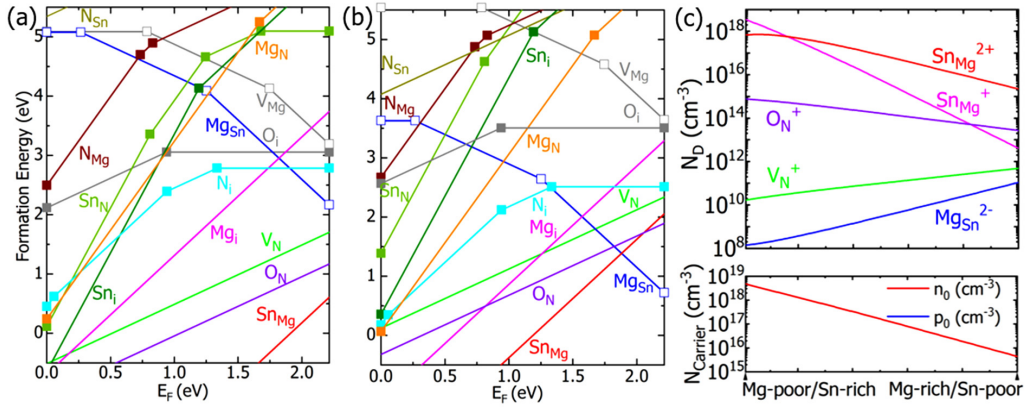


FIG. 4. Formation energy of intrinsic point defects in MgSnN_2 as a function of Fermi level (E_F) under chemical potential point A (a) and point C (b), respectively, which corresponds to Mg-poor/Sn-rich and Mg-rich/Sn-poor conditions.

procedure, we also employed the HSE-HSE procedure to calculate the formation energies of dominant donor defect Sn_{Mg} . As shown in Table I, the disparities of formation energies for 0, +1, and +2 charged Sn_{Mg} calculated by PBEsol-HSE and HSE-HSE procedures are 0.19, 0.09, and 0.01 eV. It suggests that the densities of Sn_{Mg}^0 , Sn_{Mg}^+ , and $\text{Sn}_{\text{Mg}}^{2+}$ calculated by PBEsol-HSE are slightly higher than those calculated by HSE-HSE, which would be acceptable for the evaluation of carrier densities.

On the basis of our defect calculations, changing the chemical potential of the elements, that is, from the Mg-poor/Sn-rich to the Mg-rich/Sn-poor condition, directly varies the electron densities by three orders of magnitude, which qualitatively agrees with the variation of electron densities in experimental samples. The Mg-rich/Sn-poor condition can effectively decrease the electron densities. However, this condition also gives rise to Mg_{Sn} with a deep transition level. Thus, delicately controlling chemical potential is extremely important for tuning the optoelectronic and electrical performance of MgSnN_2 . Intrinsic antisite defect Sn_{Mg} should be the dominant source of the observed high electron density in Sn-rich samples. However, the coexisting Mg, Sn metals or binary competing phases being another possible origin of the high electron density cannot be excluded.

Tuning the electron density in MgSnN_2 by varying the chemical potential of the elements, in particular, Mg and Sn, possibly leads to a cation off-stoichiometry in MgSnN_2 . Considering the low-energy intrinsic defects in MgSnN_2 , $\text{Mg}_{\text{Sn}}^{2-} + \text{Sn}_{\text{Mg}}^{2+}$, $\text{Mg}_{\text{Sn}}^{2-} + \text{Mg}_i^{2+}$, $\text{Mg}_{\text{Sn}}^{2-} + 2\text{V}_N^+$, and $\text{Mg}_{\text{Sn}}^{2-} + 2\text{O}_N^+$ are potential self-compensated defect complexes. The charge state of single point defect in defect complexes will be omitted for brevity in the discussion below. We considered various configurations of each defect

TABLE I. Formation energy (eV) of different charge states of antisite defect Sn_{Mg} under Mg-poor/Sn-rich condition with Fermi level set at VBM to exclude the influence of the disparity of band gaps.

	Sn_{Mg}^0	Sn_{Mg}^+	$\text{Sn}_{\text{Mg}}^{2+}$	E_g
PBEsol-HSE	1.32	-1.58	-3.82	2.22
HSE-HSE	1.51	-1.49	-3.83	2.35

complexes, including at least first and second nearest neighbor (NN and SNN). Additional configurations are taken into account for special defect complexes, that is, third nearest neighbor (TNN) for $\text{Mg}_{\text{Sn}} + \text{Sn}_{\text{Mg}}$, and configurations with further distance (FN) between antisite Mg_{Sn} and Mg_i for $\text{Mg}_{\text{Sn}} + \text{Mg}_i$. Cases are more complex for $\text{Mg}_{\text{Sn}} + 2\text{V}_N$ and $\text{Mg}_{\text{Sn}} + 2\text{O}_N$, thus we construct two configurations both for NN and SNN. It was identified that the configuration of NN is the most stable, as tabulated in Table II. A strong Coulomb attraction between acceptors and donors is required for the formation of stable defect complexes. As summarized in Table II, $\text{Mg}_{\text{Sn}} + \text{Sn}_{\text{Mg}}$ and $\text{Mg}_{\text{Sn}} + 2\text{O}_N$ are strongly bound with binding energy lower than -1 eV. The binding energies of $\text{Mg}_{\text{Sn}} + \text{Mg}_i$, $\text{Mg}_{\text{Sn}} + 2\text{V}_N$ are increased but still negative, indicating that $\text{Mg}_{\text{Sn}} + \text{Mg}_i$, $\text{Mg}_{\text{Sn}} + 2\text{V}_N$ can be stable once formed while they are less bound compared to $\text{Mg}_{\text{Sn}} + \text{Sn}_{\text{Mg}}$ and $\text{Mg}_{\text{Sn}} + 2\text{O}_N$.

Figure 5 displays the formation energy dependence of low-energy intrinsic point defects and defect complexes on the chemical potentials. We also compare the formation energies of neutral defect complexes with the ionized ones, and find that the neutral defect complexes are stable within the majority regime of the Fermi level and are the most stable at the calculated Fermi level under different chemical potentials.

TABLE II. Relative energies (meV/atom) of different configurations for defect complexes in MgSnN_2 and binding energies (eV) of the most stable configurations (given in parentheses).

	NN	SNN	TNN		
$\text{Mg}_{\text{Sn}} + \text{Sn}_{\text{Mg}}$	0	0.38	4.26		
	(-1.22)				
	NN	SNN	FN		
$\text{Mg}_{\text{Sn}} + \text{Mg}_i$	0	9.00	13.08		
	(-0.57)				
	NN-1	NN-2	SNN-1	SNN-2	
$\text{Mg}_{\text{Sn}} + 2\text{O}_N$	0	0.08	6.84	46.85	
	(-1.10)				
	NN-1	NN-2	SNN-1	SNN-2	
$\text{Mg}_{\text{Sn}} + 2\text{V}_N$	0.29	0	5.62	3.09	
		(-0.63)			

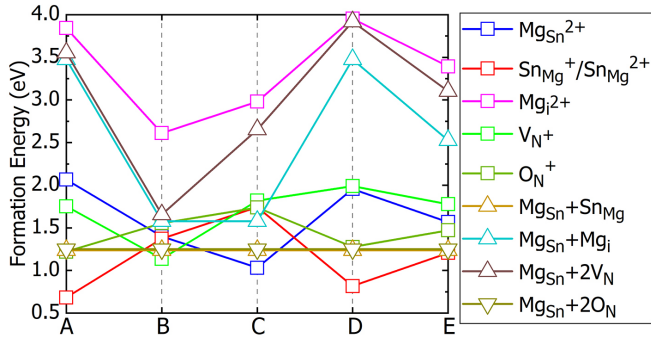


FIG. 5. Formation energy of low-energy intrinsic point defects and defect complexes in MgSnN_2 as a function of the chemical potential at points A–E shown in Fig. 2(a). The most stable charge state of these defects at the calculated Fermi level is shown. Note the formation energy of SnMg^+ is lower than that of SnMg^{2+} only at the A point.

Stoichiometry-preserving antisite pair complex $\text{Mg}_{\text{Sn}} + \text{Sn}_{\text{Mg}}$ shows the lowest formation (1.24 eV) among four possible defect complexes, as shown in Fig. 5. An appreciable population of $\text{Mg}_{\text{Sn}} + \text{Sn}_{\text{Mg}}$ is expected because of the low formation energy, which corresponds to the density $\sim 10^{14} \text{ cm}^{-3}$. Combining the characteristic of the strongly bound defect complex, the appearance of cation disorder is highly possible. We will discuss the cation disorder of MgSnN_2 in detail in Sec. III D. The formation energy of $\text{Mg}_{\text{Sn}} + 2\text{O}_\text{N}$ is merely 0.01 eV higher than that of $\text{Mg}_{\text{Sn}} + \text{Sn}_{\text{Mg}}$, denoting oxygen incorporation is unavoidable.

The formation energies of $\text{Mg}_{\text{Sn}} + \text{Mg}_\text{i}$ and $\text{Mg}_{\text{Sn}} + 2\text{V}_\text{N}$ are more sensitive to the chemical potential of the component elements (Mg/Sn ratios) than isolated intrinsic defects because they exchange more atoms with the environment. $\text{Mg}_{\text{Sn}} + \text{Mg}_\text{i}$ has a formation energy close to 1.5 eV under Mg-rich conditions [along the line BC of the chemical potential region displayed in Fig. 2(a)]. $\text{Mg}_{\text{Sn}} + \text{Mg}_\text{i}$ could appear and is a possible source of Mg off-stoichiometry. Under the Sn-rich condition, the formation energy of $\text{Mg}_{\text{Sn}} + \text{Mg}_\text{i}$ is largely increased (> 3 eV), which denotes that it is difficult to form $\text{Mg}_{\text{Sn}} + \text{Mg}_\text{i}$ defect complexes in MgSnN_2 (see Fig. 5). $\text{Mg}_{\text{Sn}} + \text{Mg}_\text{i}$ is a neutral complex, which is electrically benign in Mg-rich samples. $\text{Mg}_{\text{Sn}} + 2\text{V}_\text{N}$ has the highest formation energy among the four defect complexes within the entire chemical potential range. The chance of forming $\text{Mg}_{\text{Sn}} + 2\text{V}_\text{N}$ is even smaller than that of $\text{Mg}_{\text{Sn}} + \text{Mg}_\text{i}$.

Taken together, isolated antisite defect Sn_{Mg} plays the dominant role in the n -type doping behavior in MgSnN_2 under Mg-rich and Sn-rich conditions. Under the Mg-rich condition, isolated antisite $\text{Mg}_{\text{Sn}}^{2-}$ compensates $\text{Sn}_{\text{Mg}}^{2+}$, which reduces the electron carrier densities by an order of magnitude of 3. Additionally, there is a high chance of the formation of stoichiometry-preserving $\text{Mg}_{\text{Sn}} + \text{Sn}_{\text{Mg}}$ and oxygen involved $\text{Mg}_{\text{Sn}} + 2\text{O}_\text{N}$ defect complexes. Moreover, $\text{Mg}_{\text{Sn}} + \text{Sn}_{\text{Mg}}$ and $\text{Mg}_{\text{Sn}} + 2\text{O}_\text{N}$ are charge neutral complexes, which are beneficial for reducing the density of defect in the band gap and scattering center [68]. $\text{Mg}_{\text{Sn}} + \text{Mg}_\text{i}$ could appear in Mg-rich samples; this is also electrically benign and may cause the off-stoichiometry of the Mg element.

TABLE III. Numbers of tetrahedra of different motifs in fully ordered (FO), partially disordered, and fully disordered (FD) configurations of stoichiometric MgSnN_2 and relative energy with respect to MgSnN_2 in the FO wurtzite-type phase (ΔE).

Configuration	ΔE						(meV/atom)
	(2,2)	(3,1)	(1,3)	(4,0)	(0,4)	(4,1)	
FO	64	0	0	0	0	0	0
P-1	53	4	6	1	0	0	25
P-1 swap (a)	56	4	4	0	0	0	13
P-1 swap (b)	52	6	6	0	0	0	19
P-2	52	5	7	1	0	0	35
P-3	42	11	11	0	0	0	40
P-4	36	16	9	1	1	1	94
FD	27	15	12	4	6	0	143

D. Cation disorder in MgSnN_2

The commonly observed decreased band gap of ZnSnN_2 and ZnGeN_2 thin films is related to cation disorder [35,69,70]. For the fully ordered ternary nitrides Zn-IV-N_2 (IV = Si, Ge, Sn) in the wurtzite-type phase, the nitrogen atom in each tetrahedron is exactly coordinated with two group-II and two group-IV atoms [hereafter called a (2,2) tetrahedron], which preserves the charge neutrality and obeys the octet rule locally. It was reported that cation disorder leads to the formation of some tetrahedra having one group-II and three group-IV atoms (1,3) or three group-II and one group-IV atoms (3,1), which violate the octet rule locally but maintain the global charge neutrality by forming (3,1) and (1,3) tetrahedra elsewhere in the crystal structure [70,71]. Moreover, (4,0) or (0,4) tetrahedra which only contain four group-II or four group-IV atoms could appear in the disordered samples. We expected that cation disorder has a similar effect on the band gap of MgSnN_2 to ZnSnN_2 and ZnGeN_2 , and we studied the impact of different levels of cation disorder in MgSnN_2 . These are quantified by the ratio of tetrahedra violating the octet rule to the total number of tetrahedra (global disorder); i.e., cation disorder on the level of 17.19%, 12.50%, 18.75%, 18.75%, 34.38%, 43.75%, and 57.82% corresponds to seven disordered configurations. For simplicity, we refer to seven disordered configurations with the aforementioned levels of cation disorder to the P-1, P-1 swap (a); P-1 swap (b); P-2, P-3, P-4, and fully disorder (FD). P-1 swap (a) and P-1 swap (b) are derived from the P-1 configuration. They are constructed by eliminating the (4,0) tetrahedron manually but with global disorder close to that of the P-1 configuration as much as possible, as displayed in Table III.

As shown in Table III, configurations with an increased degree of cation disorder exhibit larger relative energies, that is, the energy difference between the P-1 swap (a) configuration and the fully ordered (FO) configuration shows the smallest value (13 meV/atom), while that between the fully disordered (FD) configuration and the FO configuration is the largest (143 meV/atom). Partially disordered configurations without (4,0) or (0,4) tetrahedra are likely to appear under growth conditions because of the small energy difference. On the contrary, the large energy difference between the FD and the FO configurations indicates that the FD sample is difficult

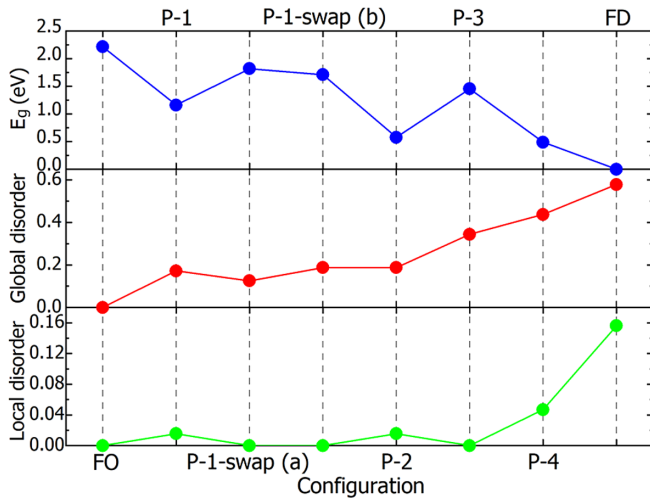


FIG. 6. Band gaps, degree of global and local disorder of fully ordered (FO), partially disordered, and fully disordered (FD) configurations of stoichiometric MgSnN_2 .

to form since it is energetically too costly. Overall, it would be challenging to synthesize MgSnN_2 samples with full long-range ordering and difficult to obtain fully disordered samples as well.

Besides the relative energies of the disordered configurations, the impact of varying the degree of cation disorder on the band gap is further investigated. Figure 6 shows the trend of the band gap as the degree of disorder varies. The band gap decreases as the degree of cation disorder increases, as can be seen from the FO, P-1, P-2, P-4, and FD configurations or the FO, P-1 swap (a), P-1 swap (b), and P-3, for which the global disorder is increased gradually (see the middle panel of Fig. 6). Among the various configurations, the FD configuration with the highest level of global disorder shows a complete closing of the band gap. Notably, besides the global disorder, local disorder [appearance of (4,0) or (0,4) tetrahedra] seems to play a role in the band-gap reduction as well. The P-2 configuration shows a smaller band gap than the P-3 configuration even though the former has a lower level of global disorder than the latter, as shown in the top and middle panels of Fig. 6. We note that there is a (4,0) tetrahedron in the P-2 configuration but no (4,0) or (0,4) tetrahedra in the P-3 configuration (see Table II), which means that the P-2 configuration exhibits a higher level of local disorder than the P-3 configuration. Moreover, if the (4,0) or (0,4) tetrahedra was eliminated, the band gap increases, as observed from the comparison between the band gaps for the P-1 and the P-1 swaps (a)/(b) configuration in Fig. 6. It is also worthwhile to note that the P-1 swap (b) and the P-2 swap have the same degree of global disorder but the latter, containing higher local disorder, shows a largely reduced band gap (0.58 eV) relative to the P-1 swap (b) (1.71 eV).

To figure out how the local disorder influences the band gap of disordered MgSnN_2 in detail, we analyze the total density of states of configurations without (4,0) and (0,4) tetrahedra and with (4,0) or (0,4) tetrahedra, respectively. Compared to the FO configuration, as shown in Fig. 7, cation disorder predominantly affects the valence band edge (VBE) of the

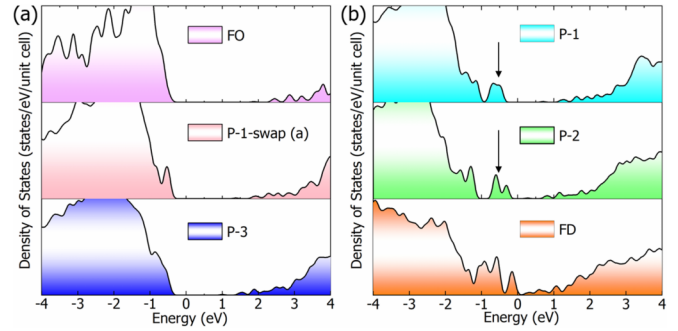


FIG. 7. Total density of states of (a) FO configuration and two cation-disordered MgSnN_2 configurations without (4,0) or (0,4) motif [P-1 swap (a) and P-3] and (b) three cation-disordered MgSnN_2 configurations with (4,0) motif (P-1, P-2, and FD).

P-1 swap (a) and the P-3 configurations without (4,0) or (0,4) tetrahedra; i.e., a defect state with low density appears around the VBE. For the P-1 and P-2 configurations containing a (4,0) tetrahedron, there is an isolated defect state, as marked by an arrow in Fig. 7(b). This local defect state leads to a large decrease of the band gap for the P-1 and P-2 configurations compared to FO, viz., 1.05 and 1.64 eV, respectively. In the FD configuration, there exists a continuum of defect states throughout the original band-gap region, thus entailing that the band gap is closed. A similar behavior is observed for the fully disordered ZnGeN_2 [71].

Figure 8(a) shows the charge density contours for the VBM and the CBM of the FO configuration; the VBM is mainly composed of N $2p$ and Sn $5d$ orbitals and the CBM is composed of N $2p$, N $2s$, and Sn $5s$ as revealed by previous studies as well [28,67]. The charge density for the VBM of the P-1 swap (a) configuration localizes at the N atom centering in the (3,1) tetrahedron and its first-neighbor (2,2) tetrahedra, whereas the charge density of the VBM of the P-1 configuration mainly localizes at the N atom centering in the (4,0) tetrahedron, as displayed in Figs. 8(b) and 8(c), respectively. The localization of charge density for the VBM of the P-1 configuration reflects the aforementioned isolated local defect state. Unlike the charge density distribution of the VBM, the charge density distribution of the CBM of the P-1 swap (a) and the P-1 configuration extends through the whole structure, suggesting that the conduction bands are less perturbed.

Ternary nitrides such as ZnSnN_2 have been suggested as photovoltaic absorbers which require a high absorption coefficient within the visible light regime. Considering the inevitable partial cation disorder in MgSnN_2 , we further studied the effect of cation disorder on the absorption spectrum. As shown in Fig. 9, the absorption coefficient of the FO configuration reaches 10^4 cm^{-3} within the 0.33 eV energy range to the onset, and then it reaches 10^5 cm^{-3} within the next 0.76 eV. For the P-1, P-1 swap (a), and P-1 swap (b) configurations, the absorption onsets shift to a lower energy because of the decreased band gaps. The behavior of optical absorption for the P-1 swap (a) and P-1 swap (b) configurations is similar to that for the FO configuration. However, the P-1 configuration shows a rather different behavior for the optical absorption; i.e., its absorption coefficient reaches 10^4 cm^{-1} within a large energy range (0.73 eV) to the absorption onset and it slowly

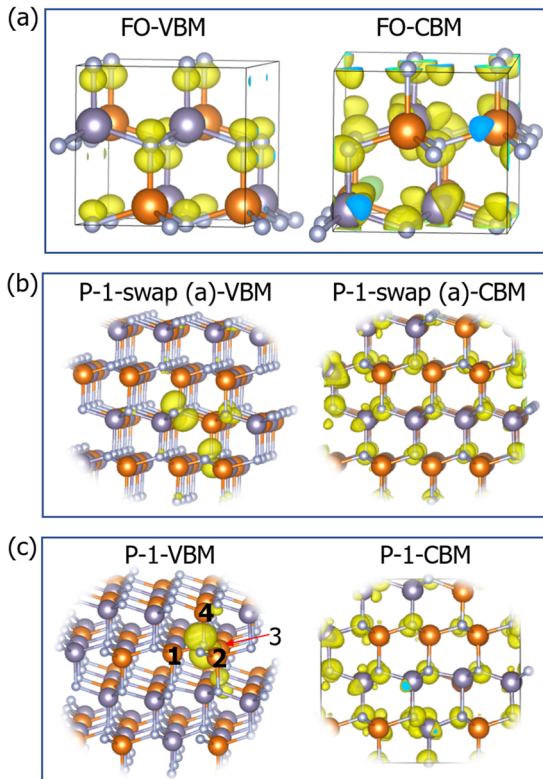


FIG. 8. Charge density contours of VBM and CBM for (a) FO, (b) P-1 swap (a), and (c) P-1 configuration. The isosurface values are $0.01 e/\text{\AA}^3$ for the VBM and $0.005 e/\text{\AA}^3$ for the CBM of the FO configurations, and $0.005 e/\text{\AA}^3$ for the VBM and $0.0005 e/\text{\AA}^3$ for the CBM of the P-1 swap (a) and P-1 configurations.

reaches 10^5 cm^{-1} within an energy range of 1.15 eV. The slow increase of the absorption coefficient should be ascribed to the isolated defect states in the P-1 configuration. Altogether, it can be seen that cation disorder results in a narrowing of the band gap and shifting the absorption onset to a lower energy, which widens the absorption energy range in the visible light spectrum. This behavior is expected to be beneficial for photovoltaic applications. Nevertheless, it is worth noting that the isolated local defect states influence the enhancement of the optical absorption because they perturb the band edge strongly, and thus the formation of (4,0) and (0,4) tetrahedra should be avoided during the preparation as far as possible.

IV. CONCLUSIONS

In this work, we study the phase stability of MgSnN_2 and ZnSnN_2 , and find that small formation enthalpy (absolute value) leads to no formation of ZnSnN_2 in the rocksalt

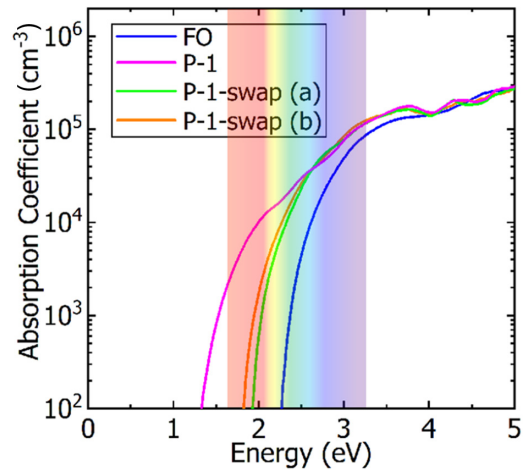


FIG. 9. Calculated absorption spectra of the FO, P-1, P-1 swap (a) and P-1 swap (b) configurations.

phase. Moreover, the higher ionicity of the Mg-N bonds compared to the Sn-N (Zn-N) bonds results in the formation of rocksalt-type MgSnN_2 under the Mg-rich condition but no appearance of MgSnN_2 under the Sn-rich condition or rocksalt-type ZnSnN_2 under the Zn-rich condition, which explains the experimental observations. In addition, via studying the defect physics of MgSnN_2 , antisite donor-type defect Sn_{Mg} is identified as the dominant source of the high electron density of MgSnN_2 . To suppress degenerated electron density, the Mg-rich/Sn-poor condition is suggested for the growth of MgSnN_2 . $\text{Mg}_{\text{Sn}} + \text{Sn}_{\text{Mg}}$ and $\text{Mg}_{\text{Sn}} + 2\text{O}_{\text{N}}$ defect complexes have a high possibility of forming. Furthermore, we systematically investigated the impact of cation disorder in MgSnN_2 by means of the cluster expansion with first-principles calculations. Stoichiometric cation disorder in MgSnN_2 induces a decrease of the band gap because of a violation of the octet rule. We find that partially disordered MgSnN_2 cannot be avoided but fully disordered MgSnN_2 is difficult to obtain under the growth conditions. The local disorder, namely, the formation of (4,0) or (0,4) tetrahedra, would lead to a large band-gap reduction and impede the enhancement of the optical absorption. Our work provides an understanding of the basic physical properties of MgSnN_2 from the theoretical aspect, which should be useful for further studies of MgSnN_2 based functional materials.

ACKNOWLEDGMENT

This work was funded by the Deutsche Forschungsgemeinschaft (DFG, German Research Foundation) under Germany's Excellence Strategy – EXC 2089/1–390776260.

- [1] H. Amano, N. Sawaki, I. Akasaki, and Y. Toyoda, *Appl. Phys. Lett.* **48**, 353 (1986).
- [2] M. Wittmer, *J. Vac. Sci. Technol., A* **3**, 1797 (1985).
- [3] H. Amano, M. Kito, K. Hiramatsu, and I. Akasaki, *Jpn. J. Appl. Phys.* **28**, L2112 (1989).
- [4] I. Akasaki, H. Amano, Y. Koide, K. Hiramatsu, and N. Sawaki, *J. Cryst. Growth* **98**, 209 (1989).

- [5] W. Saito, Y. Takada, M. Kuraguchi, K. Tsuda, I. Omura, T. Ogura, and H. Ohashi, *IEEE Trans. Electron Devices* **50**, 2528 (2003).
- [6] S. Chen, P. Narang, H. A. Atwater, and L. W. Wang, *Adv. Mater.* **26**, 311 (2014).
- [7] R. A. Makin, K. York, S. M. Durbin, N. Senabulya, J. Mathis, R. Clarke, N. Feldberg, P. Miska, C. M. Jones, Z. Deng, L.

- Williams, E. Kioupakis, and R. J. Reeves, *Phys. Rev. Lett.* **122**, 256403 (2019).
- [8] N. Feldberg, J. D. Aldous, W. M. Linhart, L. J. Phillips, K. Durose, P. A. Stampe, R. J. Kennedy, D. O. Scanlon, G. Vardar, R. L. Field *et al.*, *Appl. Phys. Lett.* **103**, 042109 (2013).
- [9] L. Lahourcade, N. C. Coronel, K. T. Delaney, S. K. Shukla, N. A. Spaldin, and H. A. Atwater, *Adv. Mater.* **25**, 2562 (2013).
- [10] W. Sun, C. J. Bartel, E. Arca, S. R. Bauers, B. Matthews, B. Orvananos, B. R. Chen, M. F. Toney, L. T. Schelhas, W. Tumas *et al.*, *Nat. Mater.* **18**, 732 (2019).
- [11] A. Punya, W. R. L. Lambrecht, and M. van Schilfgaarde, *Phys. Rev. B* **84**, 165204 (2011).
- [12] J. Häusler, S. Schimmel, P. Wellmann, and W. Schnick, *Chem. Eur. J.* **23**, 12275 (2017).
- [13] R. R. Schnepf, J. J. Cordell, M. B. Tellekamp, C. L. Melamed, A. L. Greenaway, A. Mis, G. L. Brennecke, S. Christensen, G. J. Tucker, E. S. Toberer *et al.*, *ACS Energy Lett.* **5**, 2027 (2020).
- [14] M. Ogura, D. Han, M. M. Pointner, L. S. Junkers, S. S. Rudel, W. Schnick, and H. Ebert, *Phys. Rev. Materials* **5**, 024601 (2021).
- [15] N. L. Adamski, Z. Zhu, D. Wickramaratne, and C. G. Van de Walle, *Appl. Phys. Lett.* **114**, 032101 (2019).
- [16] F. Kawamura, N. Yamada, X. Cao, M. Imai, and T. Taniguchi, *Jpn. J. Appl. Phys.* **58**, SC1034 (2019).
- [17] F. Alnjiman, S. Diliberto, J. Ghanbaja, E. Haye, S. Kassavetis, P. Patsalas, C. Gendarme, S. Bruyère, F. Cleymand, P. Miska *et al.*, *Sol. Energy Mater. Sol. Cells* **182**, 30 (2018).
- [18] T. D. Veal, N. Feldberg, N. F. Quackenbush, W. M. Linhart, D. O. Scanlon, L. F. Piper, and S. M. Durbin, *Adv. Energy Mater.* **5**, 1501462 (2015).
- [19] N. Tsunoda, Y. Kumagai, A. Takahashi, and F. Oba, *Phys. Rev. Appl.* **10**, 011001(R) (2018).
- [20] J. Fossum, R. Mertens, D. Lee, and J. Nijs, *Solid State Electron.* **26**, 569 (1983).
- [21] K. Javaid, J. Yu, W. Wu, J. Wang, H. Zhang, J. Gao, F. Zhuge, L. Liang, and H. Cao, *Phys. Status Solidi RRL* **12**, 1700332 (2018).
- [22] K. Javaid, W. Wu, J. Wang, J. Fang, H. Zhang, J. Gao, F. Zhuge, L. Liang, and H. Cao, *ACS Photonics* **5**, 2094 (2018).
- [23] Y. Wang, T. Ohsawa, X. Meng, F. Alnjiman, J.-F. Pierson, and N. Ohashi, *Appl. Phys. Lett.* **115**, 232104 (2019).
- [24] A. N. Fioretti, A. Zakutayev, H. Moutinho, C. Melamed, J. D. Perkins, A. G. Norman, M. Al-Jassim, E. S. Toberer, and A. C. Tamboli, *J. Mater. Chem. C* **3**, 11017 (2015).
- [25] A. N. Fioretti, A. Stokes, M. R. Young, B. Gorman, E. S. Toberer, A. C. Tamboli, and A. Zakutayev, *Adv. Electron. Mater.* **3**, 1600544 (2017).
- [26] M. R. Karim, B. H. D. Jayatunga, Z. Feng, K. Kash, and H. Zhao, *Cryst. Growth Des.* **19**, 4661 (2019).
- [27] N. L. Adamski, Z. Zhu, D. Wickramaratne, and C. G. Van de Walle, *Phys. Rev. B* **100**, 155206 (2019).
- [28] A. P. Jaroenjittichai and W. R. L. Lambrecht, *Phys. Rev. B* **94**, 125201 (2016).
- [29] S. Lyu and W. R. Lambrecht, *Solid State Commun.* **299**, 113664 (2019).
- [30] B. Dumre, D. Gall, and S. Khare, *J. Phys. Chem. Solids* **153**, 110011 (2021).
- [31] A. L. Greenaway, A. L. Loutris, K. N. Heinselman, C. L. Melamed, R. R. Schnepf, M. B. Tellekamp, R. Woods-Robinson, R. Sherbondy, D. Bardgett, S. Bauers *et al.*, *J. Am. Chem. Soc.* **142**, 8421 (2020).
- [32] F. Kawamura, H. Murata, M. Imura, N. Yamada, and T. Taniguchi, *Inorg. Chem.* **60**, 1773 (2021).
- [33] F. Kawamura, M. Imura, H. Murata, N. Yamada, and T. Taniguchi, *Eur. J. Inorg. Chem.* **2020**, 446 (2020).
- [34] N. Yamada, K. Matsuura, M. Imura, H. Murata, and F. Kawamura, *ACS Appl. Electron. Mater.* **3**, 1341 (2021).
- [35] M. S. Haseman, M. R. Karim, D. Ramdin, B. A. Noesges, E. Feinberg, B. H. D. Jayatunga, W. R. L. Lambrecht, M. Zhu, J. Hwang, K. Kash *et al.*, *J. Appl. Phys.* **127**, 135703 (2020).
- [36] C. L. Melamed, J. Pan, A. Mis, K. Heinselman, R. R. Schnepf, R. Woods-Robinson, J. J. Cordell, S. Lany, E. S. Toberer, and A. C. Tamboli, *J. Mater. Chem. C* **8**, 8736 (2020).
- [37] W. Kohn and L. J. Sham, *Phys. Rev.* **140**, A1133 (1965).
- [38] P. Hohenberg and W. Kohn, *Phys. Rev.* **136**, B864 (1964).
- [39] G. Kresse and J. Furthmüller, *Phys. Rev. B* **54**, 11169 (1996).
- [40] P. E. Blöchl, *Phys. Rev. B* **50**, 17953 (1994).
- [41] G. Kresse and D. Joubert, *Phys. Rev. B* **59**, 1758 (1999).
- [42] J. P. Perdew, A. Ruzsinszky, G. I. Csonka, O. A. Vydrov, G. E. Scuseria, L. A. Constantin, X. Zhou, and K. Burke, *Phys. Rev. Lett.* **100**, 136406 (2008).
- [43] D. Han, T. Zhang, M. Huang, D. Sun, M.-H. Du, and S. Chen, *APL Mater.* **6**, 084902 (2018).
- [44] J. M. Skelton, L. A. Burton, S. C. Parker, A. Walsh, C.-E. Kim, A. Soon, J. Buckeridge, A. A. Sokol, C. R. A. Catlow, A. Togo, and I. Tanaka, *Phys. Rev. Lett.* **117**, 075502 (2016).
- [45] C. N. Savory, A. M. Ganose, and D. O. Scanlon, *Chem. Mater.* **29**, 5156 (2017).
- [46] J. Pan, J. Cordell, G. J. Tucker, A. C. Tamboli, A. Zakutayev, and S. Lany, *Adv. Mater.* **31**, 1807406 (2019).
- [47] S. B. Zhang and J. E. Northrup, *Phys. Rev. Lett.* **67**, 2339 (1991).
- [48] S. H. Wei, *Comput. Mater. Sci.* **30**, 337 (2004).
- [49] D. Han, M.-H. Du, C.-M. Dai, D. Sun, and S. Chen, *J. Mater. Chem. A* **5**, 6200 (2017).
- [50] T. Rauch, F. Muñoz, M. A. L. Marques, and S. Botti, *Phys. Rev. B* **104**, 064105 (2021).
- [51] M. Huang, S.-S. Wang, Y.-N. Wu, and S. Chen, *Phys. Rev. Appl.* **15**, 024035 (2021).
- [52] S. Lany and A. Zunger, *Phys. Rev. B* **78**, 235104 (2008).
- [53] J. Ma, S.-H. Wei, T. A. Gessert, and K. K. Chin, *Phys. Rev. B* **83**, 245207 (2011).
- [54] L. Oikkonen, M. Ganchenkova, A. Seitsonen, and R. Nieminen, *J. Phys.: Condens. Matter* **26**, 345501 (2014).
- [55] S. H. Wei, L. G. Ferreira, J. E. Bernard, and A. Zunger, *Phys. Rev. B* **42**, 9622 (1990).
- [56] A. Zunger, S.-H. Wei, L. G. Ferreira, and J. E. Bernard, *Phys. Rev. Lett.* **65**, 353 (1990).
- [57] A. Van De Walle, *CALPHAD: Comput. Coupling Phase Diagrams Thermochem.* **33**, 266 (2009).
- [58] A. Punya, T. R. Paudel, and W. R. Lambrecht, *Phys. Status Solidi C* **8**, 2492 (2011).
- [59] A. Jain, G. Hautier, S. P. Ong, C. J. Moore, C. C. Fischer, K. A. Persson, and G. Ceder, *Phys. Rev. B* **84**, 045115 (2011).
- [60] A. Wang, R. Kingsbury, M. McDermott, M. Horton, A. Jain, S. P. Ong, S. Dwaraknath, and K. A. Persson, *Sci. Rep.* **11**, 1 (2021).

- [61] S. Chen, A. Walsh, X. G. Gong, and S. H. Wei, *Adv. Mater.* **25**, 1522 (2013).
- [62] D. Han, W. Ming, H. Xu, S. Chen, D. Sun, and M.-H. Du, *Phys. Rev. Appl.* **12**, 034038 (2019).
- [63] W. J. Yin, T. T. Shi, and Y. F. Yan, *Appl. Phys. Lett.* **104**, 063903 (2014).
- [64] D. O. Scanlon and G. W. Watson, *J. Phys. Chem. Lett.* **1**, 3195 (2010).
- [65] Y. Yan and S.-H. Wei, *Phys. Status Solidi B* **245**, 641 (2008).
- [66] A. N. Fioretti, J. Pan, B. R. Ortiz, C. L. Melamed, P. C. Dippo, L. T. Schelhas, J. D. Perkins, D. Kuciauskas, S. Lany, A. Zakutayev *et al.*, *Mater. Horiz.* **5**, 823 (2018).
- [67] H. M. Tang, A.-A. Sun, and S.-P. Gao, *Phys. Rev. Materials* **4**, 084004 (2020).
- [68] Y. Ke, S. Lany, J. J. Berry, J. D. Perkins, P. A. Parilla, A. Zakutayev, T. Ohno, R. O'Hayre, and D. S. Ginley, *Adv. Funct. Mater.* **24**, 2875 (2014).
- [69] A. L. Greenaway, C. L. Melamed, M. B. Tellekamp, R. Woods-Robinson, E. S. Toberer, J. R. Neilson, and A. C. Tamboli, *Annu. Rev. Mater. Res.* **51**, 591 (2021).
- [70] S. Lany, A. N. Fioretti, P. P. Zawadzki, L. T. Schelhas, E. S. Toberer, A. Zakutayev, and A. C. Tamboli, *Phys. Rev. Materials* **1**, 035401 (2017).
- [71] D. Skachkov, P. C. Quayle, K. Kash, and W. R. L. Lambrecht, *Phys. Rev. B* **94**, 205201 (2016).